

Journal of Materials Chemistry A

Accepted Manuscript



This is an *Accepted Manuscript*, which has been through the Royal Society of Chemistry peer review process and has been accepted for publication.

Accepted Manuscripts are published online shortly after acceptance, before technical editing, formatting and proof reading. Using this free service, authors can make their results available to the community, in citable form, before we publish the edited article. We will replace this *Accepted Manuscript* with the edited and formatted *Advance Article* as soon as it is available.

You can find more information about *Accepted Manuscripts* in the [Information for Authors](#).

Please note that technical editing may introduce minor changes to the text and/or graphics, which may alter content. The journal's standard [Terms & Conditions](#) and the [Ethical guidelines](#) still apply. In no event shall the Royal Society of Chemistry be held responsible for any errors or omissions in this *Accepted Manuscript* or any consequences arising from the use of any information it contains.

ARTICLE

Hierarchical I-P and I-N Porous Heterojunction in Planar Perovskite Solar Cells

Cite this: DOI: 10.1039/x0xx00000x

Hsueh-Chung Liao,^{a,b} Cheng-Si Tsao,^{*c} Meng-Huan Jao,^a Jing-Jong Shyue,^d Che-Pu Hsu,^a Yu-Ching Huang,^c Kuo-Yo Tian,^a Charn-Yin Chen,^c Chun-Jen Su,^e and Wei-Fang Su^{*a}

Received 00th January 2012,
Accepted 00th January 2012

DOI: 10.1039/x0xx00000x

www.rsc.org/

A hierarchical pore network in planar $\text{CH}_3\text{NH}_3\text{PbI}_3$ perovskite is demonstrated herein. Quantitative characterizations by grazing incidence small angle X-ray scattering (GISAXS) with modeling and complementary microscopic observations provide its insights in various length scales. It is a pore structure comprised of nano-scaled primary pores aggregating into meso-scaled fractal networks within the perovskite layer. Its structural evolution and mechanistic interpretation are explored with respect to different preparation methods / steps. The time-of-flight secondary ion mass spectrometer (TOF-SIMS) results suggest the infiltration of hole transporting materials (HTM) or electron transporting materials (ETM) deposited on top in different length scales. The inter-penetrating perovskite/HTM or perovskite/ETM form i-p or i-n one-side porous heterojunction respectively over the typically regarded planar-stacked heterojunction. They show distinctive photovoltaic characteristics and behaviors in which the large i-n interfaces in nanoscale lead to high efficiency, hysteresis-free and reliable solar cell devices. The morphology-performance correlation is helpful for associated design of device architecture and processing toward higher efficiency and stability.

Introduction

Organic / inorganic hybrid perovskite solar cells have attracted considerable attention in past few years due to its high performance and advantages of low cost, solution processability, light weight, flexibility, *etc.*¹⁻¹⁷ As compared to the current power conversion efficiencies (PCEs) of other emerging photovoltaic (PV) systems, *e.g.* (organic PV ~ 10 % and dye-sensitized solar cell (DSSC) ~ 12%, respectively),^{3, 18, 19} perovskite solar cells show exciting progress with PCE up to 19.3% (generally over 15%)^{2, 4, 6, 9, 10} in academic publication and beyond 20% in the most recently reported efficiency chart.²⁰ In the development of perovskite solar cells, two types of device structure are typically employed (1) meso-structured solar cell (MSSC) with metal-oxide serving as template scaffold for the infiltration of perovskite absorber,^{2, 5, 7, 8, 11, 21, 22} (2) p-i-n planar heterojunction (PHJ) with perovskite thin film sandwiched between p- and n- type charge collecting layer. Recently, the PHJ solar cells have delivered high PCE values >15% by integrating perovskite films in either forward structure²³⁻³⁰ or inverted structure,^{4, 6, 31-34} in which the former device collects electrons and holes by metal electrode and transparent electrode respectively and the latter device does vice versa. These significant progresses show that perovskite absorber can function with high efficiencies in simplified device architectures, favorable fabrication control, and thus toward the goal of commercialization.

The methylammonium lead halide ($\text{CH}_3\text{NH}_3\text{PbX}_3$) represents one of the most efficient hybrid perovskite materials.

It is reasonable that the mix halide with chloride doping ($\text{CH}_3\text{NH}_3\text{PbCl}_x\text{I}_{3-x}$) show high efficiency in PHJ structure owing to its long carrier/exciton diffusion length up to 1 μm which exceeds film thickness of around ~300 nm.^{26, 31, 33, 35-37} In contrast, for the triiodide perovskite $\text{CH}_3\text{NH}_3\text{PbI}_3$, shorter carrier/exciton diffusion length (~100 nm)³⁶ was reported with higher bimolecular recombination rate by an order than the mixed-halide system.^{36, 37} However, high efficiencies of PHJ solar cell with triiodide perovskite has been achieved, either in forward or inverted device structure.^{6, 23-25, 27-29, 32, 34} It was reported that the processing strategies significantly affect the device performances.^{6, 25, 32, 34} Therefore, it can be speculated that there exists a critical structure governing the mechanism and thus the device characteristics.

Additionally, to our knowledge the inverted PHJ solar cell using ETL (*e.g.* TiO_2) as substrates is under debate in perovskite research community owing to the notorious photocurrent hysteresis and mismatch of photocurrent obtained between current-voltage scanning and external quantum efficiency spectrum.³⁸⁻⁴¹ In contrast, such issues are found to be less significant in the forward PHJ solar cell using HTM as substrates but with similar solution-processed perovskite.^{24, 25, 27-30, 34} The morphology of perovskite layer and its stacking with ETL and HTL layer should play a critical role in resulting in such different photovoltaic characteristics. However, the correlations among processing, morphologies and photovoltaic performances are still not clear. To date, the structural information of perovskite obtained from scanning electron microscope (SEM) focus on the surface topography, coverage

and/or roughness, which are very limited to mechanistic understanding. In this work, we utilized grazing-incidence small-angle scattering (GISAXS) technique⁴²⁻⁴⁴ as an effective tool to quantitatively probe the nanostructures of $\text{CH}_3\text{NH}_3\text{PbI}_3$ perovskite layer in various length scales. A hierarchical pore structure within the perovskite layer is reported herein over the current structural observations. We present the existence and characterization details of nano-scaled pore structures and networks in complement with microscopic observations. Their evolution in different preparation methods / steps is explored with mechanistic interpretation. The TOF-SIMS was performed to depth mapping and profiling the infiltration of HTM (inverted structure) or ETL (forward structure). They respectively form i-p or i-n porous one-side heterojunction over the traditionally regarded planar-stacked heterojunction. We correlate the device performances and device behavior to such porous heterojunction which show distinctive photovoltaic behavior between forward (i-n) and inverted (i-p) PHJ solar cell. The results address the issues of both photocurrent hysteresis and photocurrent help the further design of highly efficient and highly stable perovskite solar cells.

Results and Discussion

In this work, we fabricated two types of layer-by-layer solar cells, i.e. forward structure and inverted structure as their configurations are shown in **Fig. 1a, 1b**, respectively. For the forward structure, poly(3,4-ethylenedioxythiophene)

polystyrene sulfonate (PEDOT:PSS) and phenyl- C_{61} -butyric acid methyl ester (PC_{61}BM) were selected as HTM and ETM respectively while in the inverted structure the perovskite layer is sandwiched between TiO_2 (ETM) and 2,2',7,7'-Tetrakis-(N,N -di-4-methoxyphenylamino)-9,9'-pirobifluorene (spiro-OMeTAD, HTM). For the processing of perovskite $\text{CH}_3\text{NH}_3\text{PbI}_3$, there are generally two methods (1) one-step method: two precursors lead iodide (PbI_2) and methylammonium iodide ($\text{CH}_3\text{NH}_3\text{I}$) are mixed and then spin-coated on substrates followed by thermal treatment^{5, 7, 45, 46} and (2) two-step method (or called sequential deposition): a PbI_2 layer is first deposited by spin-coating (Step I) which subsequently forms $\text{CH}_3\text{NH}_3\text{PbI}_3$ perovskite crystallites by reacting with $\text{CH}_3\text{NH}_3\text{I}$ solution via spin coating or immersion (Step II).^{2, 6, 23-25, 27} Generally, in PHJ solar cell the two-step method leads to remarkably higher PCE. **Fig. 1c** and **Fig. 1d** plot the current density-voltage (J-V) curves of forward and inverted PHJ solar cells respectively, which are both with one-step and two-step processed perovskite respectively. The devices are scanned in either positive direction ($V_{\text{oc}}-J_{\text{sc}}$) or negative direction ($J_{\text{sc}}-V_{\text{oc}}$), where the J_{sc} and V_{oc} denote short circuit current density and open circuit voltage respectively. Their photovoltaic characteristics are summarized in **Table 1** with statistics. Note that for one-step processed perovskite in forward structure, parts of the devices are short without photovoltage hence their statistics are not included.

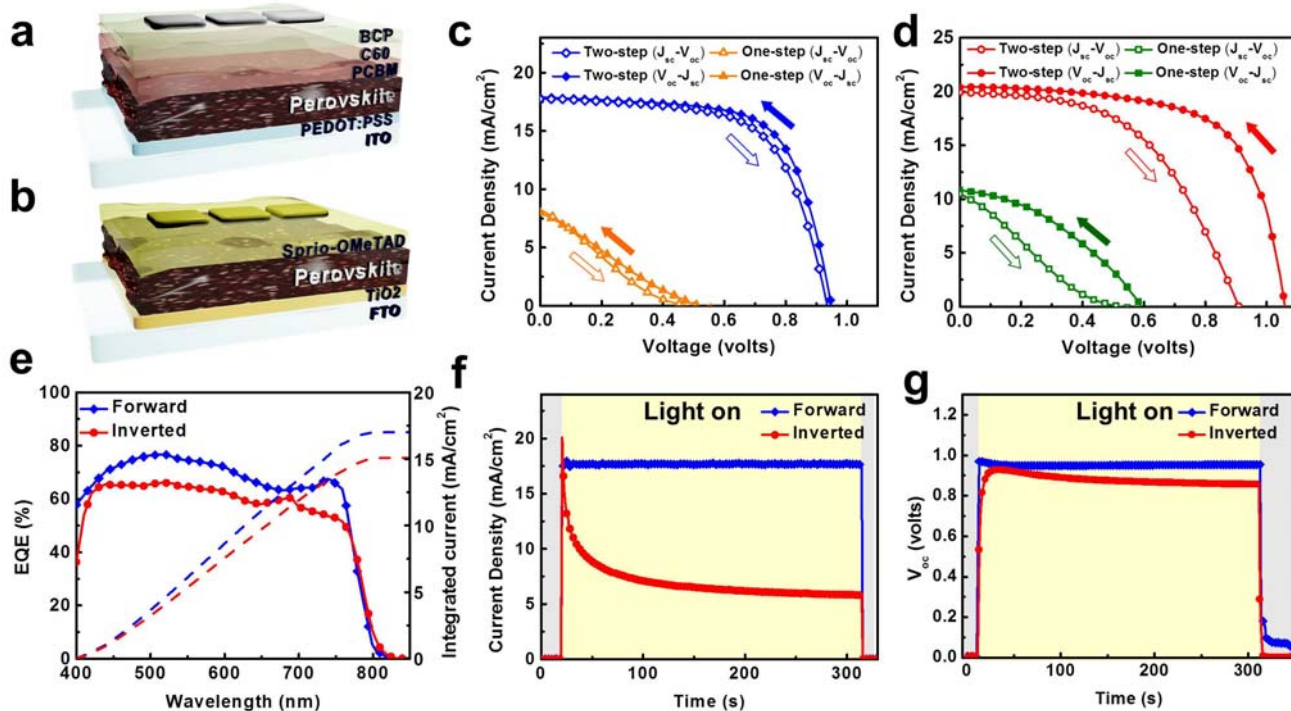


Fig. 1 a,b Illustration of PHJ solar cell in forward (a) and inverted (b) structure. c,d J-V curves of forward (c) and inverted (d) PHJ solar cell using one-step and two-step processed perovskite respectively. The dependence of scanning direction are also plotted. (e) EQE spectrum and corresponding integrated current density of forward and inverted devices with two-step processed perovskite. Photocurrent (f) and photovoltage (g) response of turning on and turning off the incident light in forward and inverted devices with two-step processed perovskite.

Table 1 Photovoltaic characteristics of forward and inverted devices with one-step and two-step processed perovskite respectively. The values in parentheses show the average PCEs and PCE distribution (standard deviation) obtained from 15 devices made from 5 independently prepared BHJ films.

Device structure	Preparation Method	Scan direction	V_{oc} (volts)	J_{sc} (mA/cm^2)	FF (%)	PCE (%)
Forward	One-step	$J_{sc} - V_{oc}$	0.51	8.1	23.5	0.97*
		$V_{oc} - J_{sc}$	0.48	7.8	20.1	0.75*
	Two-step	$J_{sc} - V_{oc}$	0.93	17.7	63.0	10.4 (9.6±1.0)
		$V_{oc} - J_{sc}$	0.95	17.7	66.0	11.1 (9.9±0.9)
Inverted	One-step	$J_{sc} - V_{oc}$	0.59	10.9	44.9	2.9 (2.2±1.2)
		$V_{oc} - J_{sc}$	0.50	10.5	20.2	1.1 (0.6±0.4)
	Two-step	$J_{sc} - V_{oc}$	0.90	19.9	50.5	9.0 (7.3±1.1)
		$V_{oc} - J_{sc}$	1.06	20.4	65.3	14.1 (13.6±0.9)

* Parts of the devices are short without photo-voltage hence their average and standard deviation of PCEs values are not presented.

Accordingly to **Table 1**, the two-step processed device exhibits remarkably higher PCE than one-step processing in both device architectures. In comparison between two different device structures, the inverted one (**Fig. 1d**) shows significance differences between positive-scanned and negative-scanned curves while such effect (*i.e.* hysteresis effect) is subtle in the forward one. Furthermore, for the forward structure the integrated current density from EQE spectrum ($\sim 17.0 \text{ mA}/\text{cm}^2$) plotted in **Fig. 1e** is consistent with the value obtained from J-V scanning (**Fig. 1c**, $17.7 \text{ mA}/\text{cm}^2$), in contrast in the inverted structure the EQE-integrated current density ($\sim 15.0 \text{ mA}/\text{cm}^2$) is much lower than that extracted from J-V scanning ($\sim 19\text{-}20 \text{ mA}/\text{cm}^2$). Such inconsistency is typically observed in inverted PHJ solar cell using TiO_2 planar substrates.^{31, 38} In literature, researchers either normalized their EQE³¹ or pre-conditioned their devices by inputting a forward bias under light soaking before EQE measurement.^{38, 47} However, such treatment is controversial for accurately evaluating the device performance for practical application. We performed the photocurrent and photovoltage tracing with turning on and turning off the light as shown in **Fig. 2f** and **2g**. Both device structures show instant response to the light on and off. In the forward device the J_{sc} ($\sim 17 \text{ mA}/\text{cm}^2$ volts) and V_{oc} (~ 0.95 volts) are steady during light-on and match the values obtained from J-V scanning (**Fig. 1c**, **Table 1**) whereas in the inverted structure both characters decay during light soaking. Specifically, the J_{sc} value read in **Fig. 1d** for inverted structure is nearly identical only to the first point of photocurrent trace (**Fig. 1f**) which then decays and stabilizes to one - third ($\sim 7 \text{ mA}/\text{cm}^2$) of the initial value after being illuminated for 300 s. This value could be the real J_{sc} for the inverted PHJ solar cell being practically used since it attains a stable out-put. It is of great interest that for MSSC with the same underlying materials, TiO_2 , but with perovskite/ TiO_2 intermixing in nanoscale, such device architecture is generally hysteresis-free and exhibits reliable photocurrent.^{39, 40} The nano- and micro-structure (morphology) of the perovskite layer could be critical accounting for this photovoltaic behavior.

The morphologies of the perovskite thin films prepared by the one-step and two-step methods were investigated by synchrotron GISAXS. **Fig. 2a** shows the GISAXS profiles, $I(Q)$, of triiodide perovskite film processed by one-step and two-step method respectively. To eliminate the effect of multiple scattering caused by the reflection and refraction beams in the grazing-incidence geometry,⁴⁸ the in-plane GISAXS profiles taken from the Yoneda peak in the measured 2D GISAXS pattern (red marked region in **Fig. 2a** inset) can be analyzed by using the conventional SAXS model.⁴⁸⁻⁵⁰ The GISAXS profiles in this study are represented by this kind of in-plane GISAXS profiles. In **Fig. 2a** the GISAXS profiles exhibit the behavior of power-law scattering ($I(Q) \propto Q^{-\alpha}$; $2.1 \leq \alpha \leq 2.6$) in the middle Q

range ($0.007 \sim 0.3 \text{ \AA}^{-1}$). The exponent values, α , reveals the typical characteristic of mass fractal. The only model, which can give the best fitting, needs to include the structure factor of fractal network comprised of the primary particles (pores in this case). Specifically, the GISAXS intensities are mainly contributed from the morphology of fractal network structure, which is formed by the aggregation of primary pores (at multi-length scales). The GISAXS intensity profile can be expressed as equation (1)

$$I_{SM}(Q) = P(Q) \cdot S(Q) \dots \dots \dots (1)$$

Where $P(Q)$ is the form factor of spherical pores as primary unit. The $S(Q)$ is the fractal structure factor, describing the interaction between primary pores in this fractal-like aggregation system. The $P(Q)$ includes a pre-factor which is the product of pore volume fraction ϕ and the square of scattering length density contrast between pore and matrix. $S(Q)$ is given by equation (2)⁵¹

$$S(Q) = 1 + \frac{\sin[(D-1)\tan^{-1}(Q\xi)]}{(QR_{SM})^D} \cdot \frac{D\Gamma(D-1)}{[1+1/(Q\xi)^2]^{(D-1)/2}} \dots \dots \dots (2)$$

Where ξ is the characteristic length of the fractal-like network domain (formed by the aggregation of the primary pores). The D is the fractal dimension. The least-squares fitting calculation of equation (1) considers the polydispersity, p , of primary pores having a Schulz size distribution with mean radius R . Note that the volume fraction values, ϕ , determined herein is only for a relative comparison rather than the absolute values because the absolute scattering contrast values cannot be measured in grazing angle configuration. The domain size of the fractal network can be approximately characterized by the Guinier radius (*i.e.*, radius of gyration: $R_g = [D(D+1)/2]^{1/2}\xi$).⁵² The obtained structural parameters are summarized in **Table 2**. The substrates used for the GISAXS experiments were Si. The concerns of substrate effect on the morphology are discussed in the **Supplementary Information, Fig. S1**). According to the structure parameters in **Table 2**, for the one-step case the difference between the fitted ξ value is not large enough to be comparable to the other fractal cases. A potential uncertainty from the limitation of SAXS model may exist to the realistic fractal system. The cut-off function as the basis of structure factor we used is the mostly used exponential cutoff.⁵³ The total interface area (including the surface area) of such fractal pore network can be determined by the Porod law⁵⁴ according to GISAXS profiles in high Q region as shown in **Fig. 2b**. (Details including the subtraction of background are shown in the **Supplementary Information**).

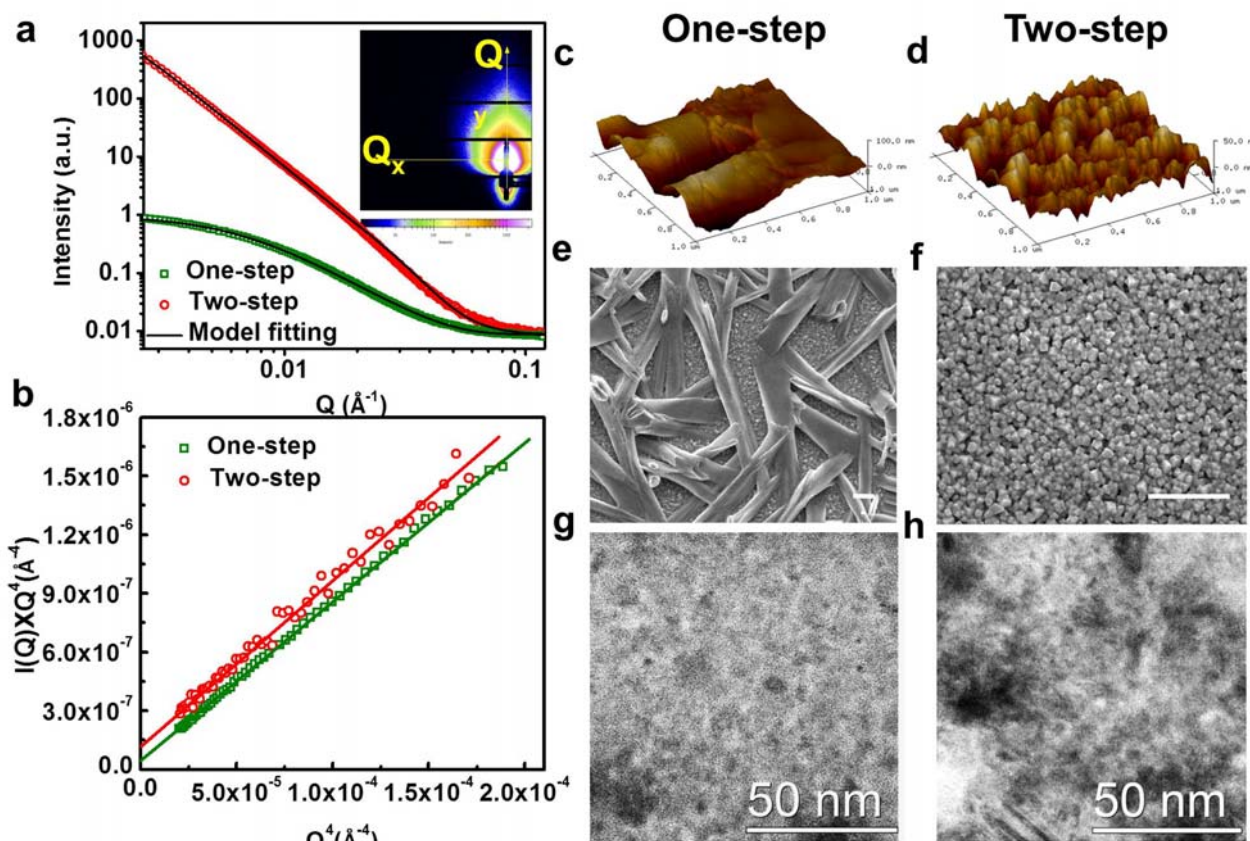


Fig. 2 Morphological characterization of one-step and two-step processed perovskite. (a) GISAXS profiles of perovskite layers prepared by one-step and two-step processing methods respectively. The inset shows the 2-D GISAXS pattern of the two-step processed perovskite with marked region (red) reduced to 1D GISAXS profile accordingly. They can be fitted by the model calculation (solid lines). (b) Plots of $Q^4 I(Q)$ vs. Q^4 from GISAXS profiles of one-step and two-step processed perovskite layer respectively. (c,d) AFM images, (e,f) SEM images and (d,f) HRTEM images of one-step and two-step processed perovskite respectively. The scale bars in the SEM images are 1 μm in length.

Within the planar perovskite thin-film prepared by one-step method (*cf.* **Table 2**), there exists a pore structure comprised of polydispersed primary pores with 3.6 nm in mean radius. The primary pores aggregate into a fractal network with fractal dimension of 2.33 and domain size ($2R_g$) of ~ 55.6 nm. The previous studies focusing on the one-step method pointed out that severe de-wetting or agglomeration occurs during perovskite crystallization on ETM.² It is consistently observed in our work as shown in **Fig. 2c** and **2e** of the atomic force microscope (AFM) image and SEM image respectively. The de-wetting feature results in incomplete coverage of perovskite with gaps between strip-like grains (μm scale in width, **Fig. 2c, 2e**). The micro-scaled gaps can be regarded as defects because they lead to direct contact between HTM and ETM and thus deteriorate the device performances. In contrast, the pore structures within the grains discovered in this study can accommodate the infiltrated ETM (forward structure) or HTM

(inverted structure) and increasing the p-i (HTM /perovskite) and n-i (ETM/perovskite) interfacial area respectively (discuss later). The HRTEM image shown in **Fig. 2g** provides the complementary observations into the strip-like grains in real space. It clearly reveals the existence of such pore structure (light color) with inter-connection into pore channels.

Regarding the perovskite film prepared by two-step method, the AFM (**Fig. 2d**) and SEM image (**Fig. 2f**) reveals distinctive meso-scale morphology as compared to the one-step processed perovskite. It can be clearly observed that the film comprised of ~ 100 nm grains which continuously pack and cover over the substrates. The meso-scale morphology is consistent with the previous observations presented by Kelly *et al.*⁶ In the present study we moreover provide insights into the structure in nanoscale inside the grains with quantitative information. Within the grains, the GISAXS results (**Table 2**)

Table 2 Structural parameters (extracted from the model fitting to GISAXS profiles) of hierarchical pore structure in the one-step and two-step processed perovskite.

Preparation method	Rel φ (%)	R (nm)	D	ξ (nm)	R_g (nm)
One-step	9	3.6	2.33	14	28
Two-step	37	5.1	2.80	120	280

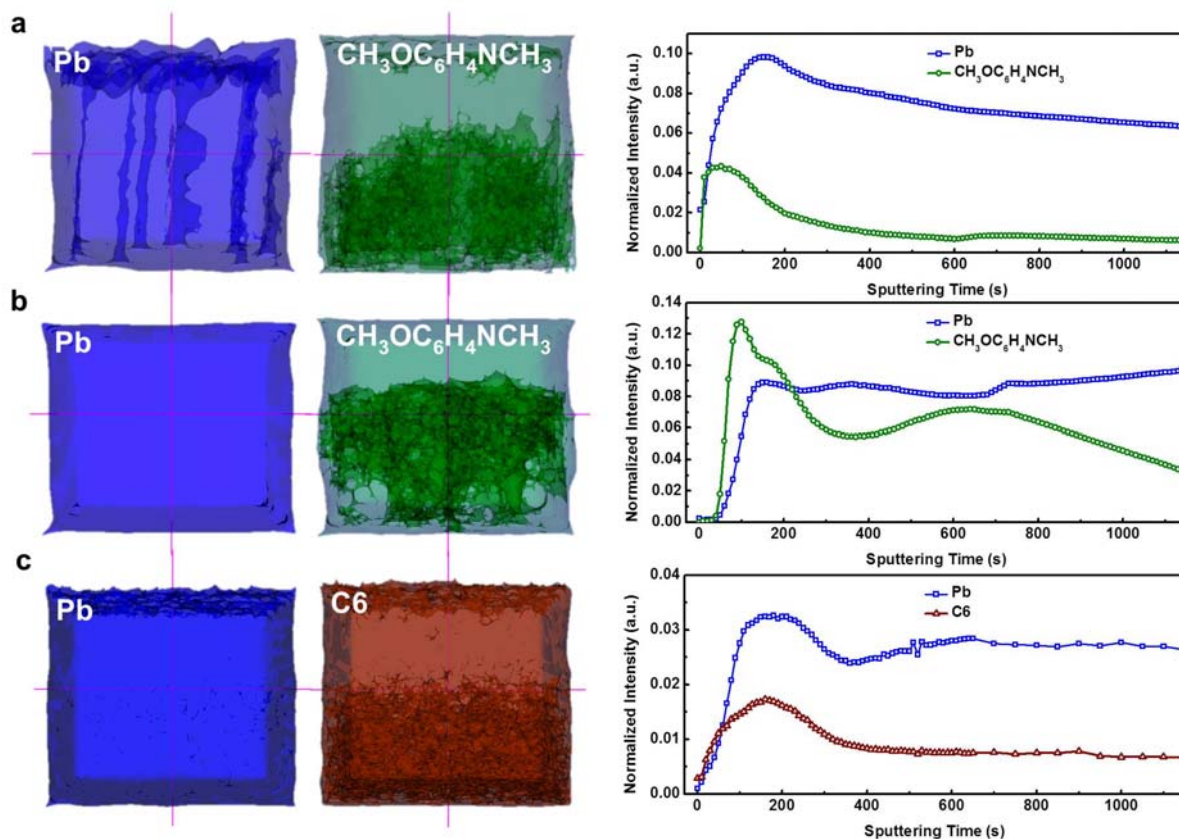


Fig. 3 TOF-SIMS intensity mapping (left images) and depth profiling (right plots) of (a) one-step processed and (b,c) two-step processed perovskite layer respectively with (a,b) HTM spiro-OMeTAD and (c) ETM PC₆₁BM spin coated on top. The Pb, CH₃OC₆H₄NCH₃ and C₆ were chosen as the representative fragments for perovskite, HTM spiro-OMeTAD, and ETM PC₆₁BM respectively. The scales of the intensity mapping images are 50 μm in width and ca. 70-100 nm in depth.

show substantially higher relative volume fraction of the pore structure ($\sim 37\%$, pore size ~ 5.1 nm in radius) than the one-step film. Additionally, the fractal dimension (D) and domain size ($2R_g$) of fractal network increases to 2.80 and 560 nm, respectively, implying that the pores connect to 3D network throughout the perovskite layer (>300 nm of layer thickness) with reduced local pore structure. Moreover, the total interface area (including the surface area) determined by the Porod law⁵⁴ (cf. **Fig. 2b** and **Supplementary Information**) is found to be higher by three times in the two-step processed perovskite than in the one-step. The above results suggest that the hierarchical pore structure take the major nanostructure within the perovskite layer. The TEM observation into the grains shown in **Fig. 2h** again supports the pore structure. It can be clearly seen that the primary pores (light color) connect to form pore channels which are surrounded by crystallites (with obvious lattice fringes).

The formation of the pore structure can be attributed to the spatial dispersion of such crystallites within the ~ 100 nm grains (discuss later). The TOF-SIMS imaging and depth profiling by *in-situ* ion sputtering were utilized to examine if the hierarchical pore structure is open to accommodate the infiltrated HTM or ETM which is deposited on top of perovskite layer in inverted and forward structure respectively. Regarding the inverted device structure, the Pb and CH₃OC₆H₄NCH₃ were chosen as the fragments for perovskite and HTM spiro-OMeTAD respectively. **Fig. 3** shows the

intensity mapping and depth profiling of Pb and CH₃OC₆H₄NCH₃ fragments for both one-step and two-step processed perovskite respectively. The CH₃OC₆H₄NCH₃ is a representative of the fragment from spiro-OMeTAD. Note that the images are in anisotropic scale, *i.e.* 50 μm along the horizontal direction and ca. 70-100 nm (according to the sputtering rate ca. 0.1 nm s⁻¹) along the vertical direction. For the one-step processed perovskite, the strip-like grains and gaps (in micro-scale) are clearly seen in the Pb fragment mapping (blue). However, such micro-scaled structures are not observed in the CH₃OC₆H₄NCH₃ fragments mapping (green). Instead, it reveals nanostructures within the perovskite. The results indicate that the HTM penetrates into the perovskite not only through the micro-scaled gaps but also through the pore structures within the micro-scaled grains. The similar nanostructures are also found in the CH₃OC₆H₄NCH₃ fragments mapping of the two-step processed sample. Distinctively, its depth profile shows a remarkable hump of CH₃OC₆H₄NCH₃ intensity, implying that larger amount of HTM infiltrates into the perovskite as compared to the one-step processed perovskite. In such two-step case, possible infiltration pathways include the pore structures within the grains or the grain boundaries as recently demonstrated by Shao et al.²⁴ It is hard to quantitatively compare the respective amounts but we deduce that the pore structure could dominate the accommodation. It is because the grain stacking in the two-step processed perovskite

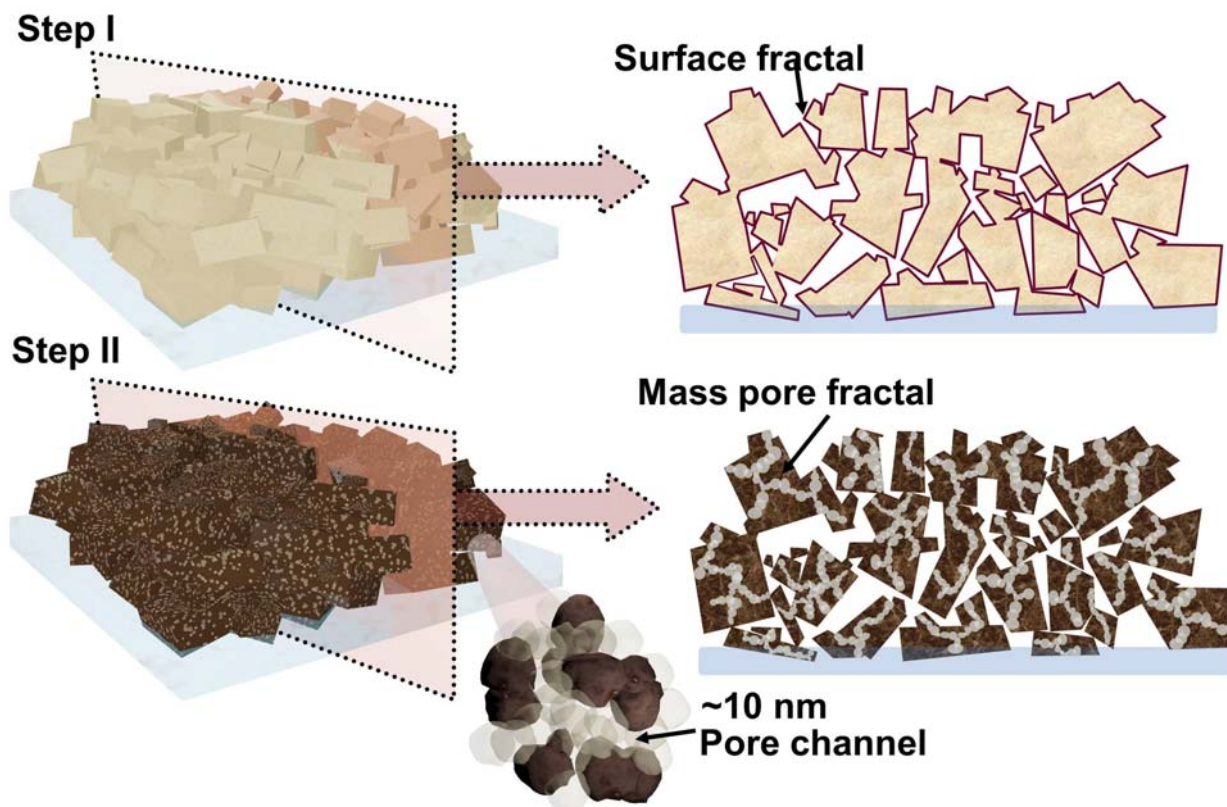


Fig. 4 Schematic illustration of two-step processed perovskite. The PbI₂ layer in step I serves as a framework with surface fractal characteristics. During step II, the porous perovskite layer is formed which is comprised of nanopores (~10 nm in diameter) interconnecting into pore channels and meso-scaled pore networks among stacked grains (~100 nm).

(Fig. 2f) is closer than the one-step processed (Fig. 2e) which shows micro-scaled gaps, however, the former case reveals larger amount of HTM infiltration (Fig. 2a and 2b). Furthermore, it is consistent with the quantitative GISAXS results (Table 2) that the volume fraction of the pore structures and total interface area (Fig. 2b and Supplementary Information) are significantly higher in the two-step processed perovskite than in the one-step. The TOF-SIMS results prove that the hierarchical pore structure is open for being able to accommodate HTM. The similar infiltration through pore structure and grain boundaries is also observed in the TOF-SIMS mapping and depth profiling (Fig. 3c) of two-step processed perovskite in forward structure in which the PC₆₁BM was spin coated on the top of perovskite layer. The C6 fragment was used to represent PC₆₁BM.

Mechanistic understanding in the formation of the hierarchical pore structure is discussed as follows. We mainly focus on the two-step process owing to the minor role of pore structure (low volume fraction, Table 2) and significant dewetting in one-step processed perovskite. The GISAXS profile of the PbI₂ layer (step-I of the two-step processing) is plotted in the Supplementary Information. The profile shows a fractal dimension of $\alpha = 3.6$ ($I(Q) \propto Q^{-\alpha}$; $3 \leq \alpha (= 3.6) \leq 4$) which reveals the characteristic of surface fractal morphology at different scales and little internal pore network. This indicates that the dipping of CH₃NH₃I in step-II leads to the transition from surface fractal scattering of PbI₂ to pore mass fractal scattering of perovskite CH₃NH₃PbI₃. It can be speculated that the CH₃NH₃I solution diffuses from the surface of PbI₂ framework into the interior which enables the crystallization of

CH₃NH₃PbI₃. The X-ray diffraction (XRD) patterns of PbI₂ film (Step I) and perovskite (Step II) (Supplementary Information) suggests the nearly complete transformation after dipping in CH₃NH₃I solution for 40s. Therefore, the dispersion/construction of perovskite crystallites within the grains (~100 nm) leaves the fractal pore network and its spatial distribution are likely to extend from the surface entry pores or boundary gaps between PbI₂ grains which gradually decreases along the vertical depth direction. This results in a favorable diffusion-like percolation network or porous structure. In short conclusion, the PbI₂ film can serve as a framework with a high-contact-area fractal surface structure. Afterwards, an open, penetrating and internal pore network forms during the step-II for the following HTM or ETM infiltration. According to the quantitative morphological investigations shown above, the 3D and 2D nanostructures of such hierarchical porous perovskite and its associated evolution during two-step processing can be illustrated in Fig. 4 in various length scales.

Considering the CH₃NH₃PbI₃ is an intrinsic semiconductor, the infiltration of HTM or ETM into pore structure throughout the perovskite layer form i-p or i-n porous heterojunction. This percolation in nanoscale attributes to the high efficiency of CH₃NH₃PbI₃ PHJ although its exciton/carrier diffusion length (~100 nm) is one-third of film thickness (~300 nm).³⁵ Specifically, the inter-mixing of perovskite/HTM or perovskite/ETM is in different length scales, from primary pores of ~10 nm, grain boundaries ~ tens of nanometers, to pore channel and network of hundreds of nanometers, which is a typical characteristic of fractal structure (i.e. hierarchical heterojunction). Such i-p or i-n one-side junction not only

provides substantial interfacial area for carrier collection, but influences the photovoltaic behavior. It has been recently reported that the PC₆₁BM could successfully passivate the defect density state of perovskite and hence release the hysteresis.²⁴ We consistently observe in our work that the forward structure shows hysteresis-free and reliable short-circuit current (Fig. 1) owing to the inter-penetration of PC₆₁BM and perovskite in nanoscale. Such i-n (perovskite/PC₆₁BM) heterojunction structure is analogous to the MSSC in which the TiO₂ nanoparticles (~20 nm) are inter-mixed with perovskite crystallites in nanoscale and reveal reliable photovoltaic behavior.^{39,40} In contrast, for the inverted PHJ with i-p one side junction, the electron collection only relies on the planar contact between perovskite layer and TiO₂ compact layer. Recent work done by Edri et al. pointed out that in perovskite the diffusion length of electron is shorter than the hole.^{55, 56} High efficient HTM-free devices can be as the perovskite itself is a good hole conductor.⁵⁷⁻⁶¹ Therefore, the present work further elucidate why large i-n interfaces are essential to achieve high efficient, hysteresis-free and reliable perovskite solar cell devices from the morphological point of view. The i-n porous heterojunction would be the target of ideal design toward high performance in the future.

Conclusions

We demonstrate the hierarchical pore structure at different length scales in PHJ CH₃NH₃PbI₃ perovskite solar cells. Its structural information is presented quantitatively, from primary pores to their aggregation into fractal network at nano- and meso-scale, by GISAXS analysis with complementary morphological observation including SEM, TEM, AFM, *etc.* The pore structure formed in two-step processed perovskite takes the majority with relatively high volume fraction and large-scaled network. The HTM or ETM was found to in-depth infiltrate through such porous structures through different length scales. An i-p (perovskite/HTM) or i-n (perovskite/PC₆₁BM) one-side hierarchical porous heterojunction can be formed which play crucial role in photovoltaic behaviors. Larger i-n interfaces are essential to passivate the hysteresis and stable out-put photocurrent and hence attain high efficiency and reliable solar cell performance. The morphological insights and associated mechanistic interpretation and correlation with device performances are presented herein which informatively guide the rational strategies for further processing high efficiency perovskite solar cells.

Experimental

Solar cell device fabrication

For the inverted device, fluorine doped tin oxide (FTO) substrate was ultrasonically cleaned by a series of solvents, DI water, ammonium/deionized water/hydrogen peroxide, methanol, and isopropanol followed by oxygen plasma treatment for 15 minutes. A TiO₂ sol-gel solution (Catalog No. AA, FrontMaterials. Co. Ltd.) was spin coated on FTO at 1000 rpm for 40 s and sintered at 500°C for 30 minutes. The obtained FTO/TiO₂ substrate was transferred into a humidity box with relative control of 3% for the following perovskite layer processing. For the one-step processing, PbI₂ (Catalog No. 19886, ACROS) and methylammonium iodide (CH₃NH₃I, Catalog No. BA, FrontMaterials. Co. Ltd.) in a weight ratio of 3:1 was dissolved in N,N-dimethylformamide with a

concentration of 40 wt%. The solution was stirred at 50°C overnight and spin coated on the FTO/TiO₂ substrate at 2000 rpm for 30s. Subsequently, the perovskite thin film was thermal annealed at 100°C for 2 minutes. The film color changed from yellow to dark brown during thermal treatment. For the two step processing, PbI₂ (460 mg/ml in N,N-dimethylformamide) was first spin coated on FTO/TiO₂ substrate at 3000 rpm for 15s followed by thermal annealing at 70 °C for 10 minutes. The PbI₂ film was then dipped into CH₃NH₃I solution (45 mg/ml in isopropanol) filled in a petri dish for 40 s. The film color changed from yellow to dark brown immediately after immersion. The obtained perovskite film was rinsed with isopropanol and dried by N₂ flow and thermal annealed at 100°C for 2 hours. The hole transporting materials (HTM) Spiro-OMeTAD (Catalog No. EA, FrontMaterials Co. Ltd.) doped with 28.5 μl 4-tertbutylpyridine and 17.5μl lithium-bis(trifluoromethanesulfonyl)imide (Li-TFSI) chlorobenzene (80 mg / ml) was spin coated at 4000 rpm for 30 s. The Au electrode was then thermal evaporated to finish the solar cell device with an active area of 0.09 cm². For the forward structure, PEDOT:PSS (Baytron-P 4083) layer was spin coated on cleaned indium tin oxide (ITO) glass at 6000 rpm for 40 s followed by thermal annealing at 130°C for 15 mins. The depositions of perovskite layer for one-step and two-step process were identical to the procedures described in the inverted structure. Subsequently, PC₆₁BM (American Dye Source) with concentration of 20 mg/ml in chlorobenzene was spin coated on the perovskite layer at 1000 rpm for 40 s. The devices were completed by thermal evaporation C₆₀ (20 nm), BCP (8 nm) and Al (100 nm) with active area of 0.06 cm². The devices were tested in air with a shadow mask of 0.12 cm² and 0.08 cm² for inverted and forward devices respectively. The PCEs and photocurrent / photovoltage tracing were characterized under A.M. 1.5 radiation (100 mW / cm²) of a solar simulator source (Newport Inc.) and recorded by Keithley 2400 source meter.

Morphological characterizations

The GISAXS measurement was performed at beam line 23A of NSRRC, Taiwan. The experimental configuration can be found in our previous work.⁴²⁻⁴⁴ Briefly, the one-step and two-step processed perovskite were spin-coated on Si substrates and Si/TiO₂ substrates respectively. Note that the processing conditions of compact TiO₂ film and perovskite layer were identical to those used in solar cell device fabrication. The monochromated X-ray beam (10 keV, wavelength = 1.24 Å, incidence angle = 0.2°) was used to characterize the sample films. The 2-D GISAXS patterns were collected by a 2-D area detector (Pilatus, 7 ms/frame, 169mm by 179 mm) with sample-to-detector distance of 511 cm. The 1-D GISAXS profiles were obtained by reducing the 2-D patterns along the in-plane direction with background subtraction according to the sample film transmission, *i.e.* the ratio of the specular beam intensities between sample on substrate and pure substrate in the identical GISAXS geometry. The TEM samples were prepared by utilizing focused ion beam (FEI Helios 600i) slicing vertically along the solar cell device. The samples were with thickness < 100 nm. The TEM images were obtained from FEI Tecnai G2 T20 microscope operating at 200 KeV. The meso-scaled morphologies were observed by SEM (JEOL JSM-6500F). The powder XRD was performed at a X-ray diffractometer (PANalytical X'Pert PRO) radiated by Cu K α (wavelength = 1.54 Å). The topographic observation was analysed by AFM (Digital Instruments, Nanoscopes III).

ToF-SIMS measurements

The TOF-SIMS was performed with a PHI TRIFT V nanoTOF (Chigasaki, Japan) ToF-SIMS system. The pulsed primary ion source was Bi⁺ and was operated at 30 kV (1 nA DC) with a 50 μm × 50 μm rastering area (256 × 256 scattered pixels with ~200 nm beam size) at an incident angle of 40°. The pulse width was about 10 ns and the m/z of primary beam was selected using a double pulser system. The pulse rate is 7950 Hz and the acquisition dosage is ~1.2 × 10¹² ion/cm². The analyzer collects positively charged secondary ions with 240 eV pass-band from a direction that is normal to the specimen surface. The mass resolution of [H₃COC₆H₄NCH₃]⁺ (136.0762) is ~7000 m/Δm. A 10 V pulsed flooding electron beam was used for charge compensation. Ar cluster ion is generated by adiabatic expansion from 640 kPa. The depth profile is done by Wien-filtered Ar₂₅₀₀⁺ ion beam operated at 10 kV and 5 nA with a 1000 μm × 1000 μm rastering area at an incident angle of 40°.

Acknowledgements

Financial supports obtained from Ministry of Science and Technology of Taiwan (Project 102-3113-P-002-027) and Institute of Nuclear Energy Research (Projects 103-S-A18) are highly appreciated.

Notes and references

- ^a No. 1, Sec. 4, Roosevelt Road, Department of Materials Science and Engineering, National Taiwan University, Taipei 10617, Taiwan
 Fax: +886 2 33664078; Tel: +886 2 33664078; E-mail: suwf@ntu.edu.tw
- ^b No. 2-3, Ln. 66, Zhulin Rd., Yonghe Dist., New Taipei City 23441, Taiwan, FrontMaterials Co. Ltd.
- ^c No. 1000, Wenhua Road, Institute of Nuclear Energy Research, Longtan Township, Taoyuan County 32546, Taiwan
 Tel: +886 3 4711400 ext. 3420; E-mail: cstsao@iner.gov.tw
- ^d No. 128, Academia Road, Section 2, Academia Sinica, Nankang, Taipei 115, Taiwan
- ^e No. 101, Hsin-An Road, National Synchrotron Radiation Research Center, Hsinchu 300-77, Taiwan
- † Electronic Supplementary Information (ESI) available: Effect of substrate on the GISAXS experiments; Interface (Surface) area determined by Porod's law. GISAXS profiles of two-step processing of PbI₂ layer (step I) and perovskite layer. 1D XRD pattern of PbI₂ and two-step processed perovskite. See DOI: 10.1039/b000000x/
1. P. Docampo, J. M. Ball, M. Darwich, G. E. Eperon and H. J. Snaith, *Nat. Commun.*, 2013, **4**, 2761.
 2. J. Burschka, N. Pellet, S. J. Moon, R. Humphry-Baker, P. Gao, M. K. Nazeeruddin and M. Grätzel, *Nature*, 2013, **499**, 316-319.
 3. I. Chung, B. Lee, J. He, R. P. Chang and M. G. Kanatzidis, *Nature*, 2012, **485**, 486-489.
 4. M. Liu, M. B. Johnston and H. J. Snaith, *Nature*, 2013, **501**, 395-398.
 5. J. H. Heo, S. H. Im, J. H. Noh, T. N. Mandal, C.-S. Lim, J. A. Chang, Y. H. Lee, H.-j. Kim, A. Sarkar, M. K. Nazeeruddin, M. Grätzel and S. I. Seok, *Nat. Photonics*, 2013, **7**, 486-491.
 6. D. Liu and T. L. Kelly, *Nat. Photonics*, 2013, **8**, 133-138.
 7. H. S. Kim, C. R. Lee, J. H. Im, K. B. Lee, T. Moehl, A. Marchioro, S. J. Moon, R. Humphry-Baker, J. H. Yum, J. E. Moser, M. Grätzel and N. G. Park, *Sci. Rep.*, 2012, **2**, 591.
 8. M. M. Lee, J. Teuscher, T. Miyasaka, T. N. Murakami and H. J. Snaith, *Science*, 2012, **338**, 643-647.
 9. H. Zhou, Q. Chen, G. Li, S. Luo, T. B. Song, H. S. Duan, Z. Hong, J. You, Y. Liu and Y. Yang, *Science*, 2014, **345**, 542-546.
 10. J. H. Im, I. H. Jang, N. Pellet, M. Grätzel and N. G. Park, *Nat. Nanotechnol.*, 2014, **9**, 927-932.

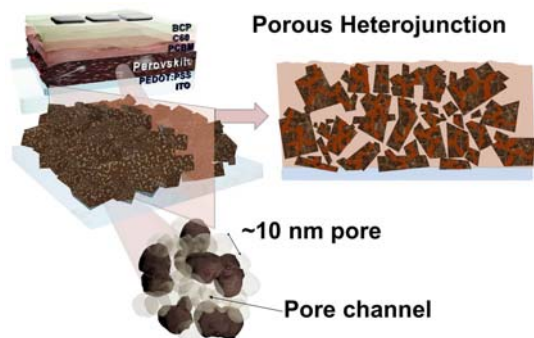
11. N. J. Jeon, J. H. Noh, Y. C. Kim, W. S. Yang, S. Ryu and S. I. Seok, *Nat. Mater.*, 2014, **13**, 897-903.
12. J. B. You, Z. R. Hong, Y. Yang, Q. Chen, M. Cai, T. B. Song, C. C. Chen, S. R. Lu, Y. S. Liu, H. P. Zhou and Y. Yang, *ACS Nano*, 2014, **8**, 1674-1680.
13. G. E. Eperon, V. M. Burlakov, A. Goriely and H. J. Snaith, *ACS Nano*, 2014, **8**, 591-598.
14. K. W. Tan, D. T. Moore, M. Saliba, H. Sai, L. A. Estroff, T. Hanrath, H. J. Snaith and U. Wiesner, *ACS Nano*, 2014, **8**, 4730-4739.
15. S. Kazim, M. K. Nazeeruddin, M. Grätzel and S. Ahmad, *Angew. Chem. Int. Ed.*, 2014, **53**, 2812-2824.
16. H. J. Snaith, *J. Phys. Chem. Lett.*, 2013, **4**, 3623-3630.
17. H. S. Jung and N. G. Park, *Small*, 2015, **11**, 10-25.
18. J. You, L. Dou, K. Yoshimura, T. Kato, K. Ohya, T. Moriarty, K. Emery, C. C. Chen, J. Gao, G. Li and Y. Yang, *Nature Commun.*, 2013, **4**, 1446.
19. A. Yella, H. W. Lee, H. N. Tsao, C. Yi, A. K. Chandiran, M. K. Nazeeruddin, E. W. Diau, C. Y. Yeh, S. M. Zakeeruddin and M. Grätzel, *Science*, 2011, **334**, 629-634.
20. M. A. Green, K. Emery, Y. Hishikawa, W. Warta and E. D. Dunlop, *Prog. Photovoltaics*, 2015, **23**, 1-9.
21. P. Qin, S. Paek, M. I. Dar, N. Pellet, J. Ko, M. Grätzel and M. K. Nazeeruddin, *J. Am. Chem. Soc.*, 2014, **136**, 8516-8519.
22. D. Nanova, A. K. Kast, M. Pfannmoller, C. Muller, L. Veith, I. Wacker, M. Agari, W. Hermes, P. Erk, W. Kowalsky, R. R. Schroder and R. Lovrincic, *Nano Lett.*, 2014, **14**, 2735-2740.
23. Z. L. Zhu, Y. Bai, T. Zhang, Z. K. Liu, X. Long, Z. H. Wei, Z. L. Wang, L. X. Zhang, J. N. Wang, F. Yan and S. H. Yang, *Angew. Chem. Int. Ed.*, 2014, **53**, 12571-12575.
24. Y. Shao, Z. Xiao, C. Bi, Y. Yuan and J. Huang, *Nat Commun*, 2014, **5**, 5784.
25. C.-H. Chiang, Z.-L. Tseng and C.-G. Wu, *J. of Mater. Chem. A*, 2014, **2**, 15897-15903.
26. A. T. Barrows, A. J. Pearson, C. K. Kwak, A. D. F. Dunbar, A. R. Buckley and D. G. Lidzey, *Energy Environ. Sci.*, 2014, **7**, 2944.
27. D. Zhao, M. Sexton, H.-Y. Park, G. Baure, J. C. Nino and F. So, *Adv. Energy Mater.*, 2014, DOI: 10.1002/aenm.201401855.
28. J. Y. Jeng, K. C. Chen, T. Y. Chiang, P. Y. Lin, T. D. Tsai, Y. C. Chang, T. F. Guo, P. Chen, T. C. Wen and Y. J. Hsu, *Adv. Mater.*, 2014, **26**, 4107-4113.
29. J. H. Kim, P. W. Liang, S. T. Williams, N. Cho, C. C. Chueh, M. S. Glaz, D. S. Ginger and A. K. Jen, *Adv. Mater.*, 2014, **27**, 695-701.
30. W. Nie, H. Tsai, R. Asadpour, J.-C. Blancon, A. J. Neukirch, G. Gupta, J. J. Crochet, M. Chhowalla, S. Tretiak, M. A. Alam, H.-L. Wang and A. D. Mohite, *Science*, 2015, **347**, 522-525.
31. H. Zhou, Q. Chen, G. Li, S. Luo, T. B. Song, H. S. Duan, Z. Hong, J. You, Y. Liu and Y. Yang, *Science*, 2014, **345**, 542-546.
32. M. Xiao, F. Huang, W. Huang, Y. Dkhissi, Y. Zhu, J. Etheridge, A. Gray-Weale, U. Bach, Y. B. Cheng and L. Spiccia, *Angew. Chem. Int. Ed.*, 2014, **53**, 9898-9903.
33. G. E. Eperon, V. M. Burlakov, P. Docampo, A. Goriely and H. J. Snaith, *Adv. Funct. Mater.*, 2014, **24**, 151-157.
34. Q. Chen, H. Zhou, Z. Hong, S. Luo, H. S. Duan, H. H. Wang, Y. Liu, G. Li and Y. Yang, *J. Am. Chem. Soc.*, 2014, **136**, 622-625.
35. S. D. Stranks, G. E. Eperon, G. Grancini, C. Menelaou, M. J. Alcocer, T. Leijtens, L. M. Herz, A. Petrozza and H. J. Snaith, *Science*, 2013, **342**, 341-344.
36. C. Wehrenfennig, G. E. Eperon, M. B. Johnston, H. J. Snaith and L. M. Herz, *Adv. Mater.*, 2014, **26**, 1584-1589.
37. T. C. Sum and N. Mathews, *Energy Environ. Sci.*, 2014, **7**, 2518-2534.
38. E. L. Unger, E. T. Hoke, C. D. Bailie, W. H. Nguyen, A. R. Bowring, T. Heumüller, M. G. Christoforo and M. D. McGehee, *Energy Environ. Sci.*, 2014, **7**, 3690-3698.
39. N. J. Jeon, J. H. Noh, Y. C. Kim, W. S. Yang, S. Ryu and S. I. Seok, *Nat. Mater.*, 2014, **13**, 897-903.
40. M. D. McGehee, *Nat. Mater.*, 2014, **13**, 845-846.
41. K. Wojciechowski, S. D. Stranks, A. Abate, G. Sadoughi, A. Sadhanala, N. Kopidakis, G. Rumbles, C. Z. Li, R. H. Friend, A. K. Y. Jen and H. J. Snaith, *ACS Nano*, 2014, **8**, 12701-12709.

42. H. C. Liao, C. S. Tsao, T. H. Lin, M. H. Jao, C. M. Chuang, S. Y. Chang, Y. C. Huang, Y. T. Shao, C. Y. Chen, C. J. Su, U. S. Jeng, Y. F. Chen and W. F. Su, *ACS Nano*, 2012, **6**, 1657-1666.
43. H. C. Liao, C. S. Tsao, T. H. Lin, C. M. Chuang, C. Y. Chen, U. S. Jeng, C. H. Su, Y. F. Chen and W. F. Su, *J. Am. Chem. Soc.*, 2011, **133**, 13064-13073.
44. H.-C. Liao, C.-S. Tsao, Y.-T. Shao, S.-Y. Chang, Y.-C. Huang, C.-M. Chuang, T.-H. Lin, C.-Y. Chen, C.-J. Su, U. S. Jeng, Y.-F. Chen and W.-F. Su, *Energy Environ. Sci.*, 2013, **6**, 1938.
45. J. H. Im, C. R. Lee, J. W. Lee, S. W. Park and N. G. Park, *Nanoscale*, 2011, **3**, 4088-4093.
46. A. Kojima, K. Teshima, Y. Shirai and T. Miyasaka, *J. Am. Chem. Soc.*, 2009, **131**, 6050-6051.
47. J. M. Ball, S. D. Stranks, M. T. Hörlantner, S. Hüttner, W. Zhang, E. J. W. Crossland, I. Ramirez, M. Riede, M. B. Johnston, R. H. Friend and H. J. Snaith, *Energy Environ. Sci.*, 2015, **8**, 602-609.
48. G. Renaud, R. Lazzari and F. Leroy, *Surf. Sci. Rep.*, 2009, **64**, 255-380.
49. T. R. Andersen, T. T. Larsen-Olsen, B. Andreasen, A. P. L. Bottiger, J. E. Carle, M. Helgesen, E. Bundgaard, K. Norrman, J. W. Andreasen, M. Jorgensen and F. C. Krebs, *ACS Nano*, 2011, **5**, 4188-4196.
50. C. Y. Chen, C. S. Tsao, Y. C. Huang, H. W. Liu, W. Y. Chiu, C. M. Chuang, U. S. Jeng, C. J. Su, W. R. Wu, W. F. Su and L. Wang, *Nanoscale*, 2013, **5**, 7629-7638.
51. S. R. Kline, *J. Appl. Crystallogr.*, 2006, **39**, 895-900.
52. J. Teixeira, *J. Appl. Crystallogr.*, 1988, **21**, 781-785.
53. S. H. Chen and J. Teixeira, *Phys. Rev. Lett.*, 1986, **57**, 2583-2586.
54. G. Laudisio, R. K. Dash, J. P. Singer, G. Yushin, Y. Gogotsi and J. E. Fischer, *Langmuir*, 2006, **22**, 8945-8950.
55. E. Edri, S. Kirmayer, A. Henning, S. Mukhopadhyay, K. Gartsman, Y. Rosenwaks, G. Hodes and D. Cahen, *Nano Lett.*, 2014, **14**, 1000-1004.
56. E. Edri, S. Kirmayer, S. Mukhopadhyay, K. Gartsman, G. Hodes and D. Cahen, *Nat. Commun.*, 2014, **5**.
57. S. Aharon, B. E. Cohen and L. Etgar, *J. Phys. Chem. C*, 2014, **118**, 17160-17165.
58. L. Etgar, P. Gao, Z. Xue, Q. Peng, A. K. Chandiran, B. Liu, M. K. Nazeeruddin and M. Gratzel, *J. Am. Chem. Soc.*, 2012, **134**, 17396-17399.
59. J. Shi, J. Dong, S. Lv, Y. Xu, L. Zhu, J. Xiao, X. Xu, H. Wu, D. Li, Y. Luo and Q. Meng, *Appl. Phys. Lett.*, 2014, **104**, 063901.
60. W. A. Laban and L. Etgar, *Energy Environ. Sci.*, 2013, **6**, 3249.
61. A. Y. Mei, X. Li, L. F. Liu, Z. L. Ku, T. F. Liu, Y. G. Rong, M. Xu, M. Hu, J. Z. Chen, Y. Yang, M. Gratzel and H. W. Han, *Science*, 2014, **345**, 295-298.

Table of Content

Hierarchical I-P and I-N Porous Heterojunction in Planar Perovskite Solar Cells

Hsueh-Chung Liao,^{a,b} Cheng-Si Tsao,^{*c} Meng-Huan Jao,^a Jing-Jong Shyue,^d Che-Pu Hsu,^a Yu-Ching Huang,^c Kuo-Yo Tian,^a Charn-Yin Chen,^c Chun-Jen Su,^e and Wei-Fang Su^{*a}



A hierarchical pore networks is discovered in $\text{CH}_3\text{NH}_3\text{PbI}_3$ perovskite solar cell which forms i-p or i-n porous heterojunction with infiltrated hole transporting materials or electron transporting materials respectively. Their morphological insights and associated influences in photovoltaic behaviour are presented in this work.